Supplementary Information: text

A specific demetalation of Fe-N$_4$ catalytic sites in the micropores of NC_Ar+NH$_3$ is at the origin of the initial activity loss of this highly active Fe/N/C catalyst used for the reduction of oxygen in PEM fuel cell

Régis Chenitz[a], Ulrike Kramm[b], Michel Lefèvre[c], Vassili Glibin[d], Gaixia Zhang[a], Shuhui Sun[a], Jean-Pol Dodelet[a,*]

a : INRS-Énergie, Matériaux et Télécommunications, 1650 Boulevard Lionel Boulet, Varennes, Québec, Canada, J3X 1S2

b : TU Darmstadt, Graduate School Energy Science and Engineering, Department of Materials- and Earth Sciences and Department of Chemistry, Otto-Berndt-Str. 3, 64287 Darmstadt, Germany

c : Canetique Electrocatalysis, 1650 Boulevard Lionel Boulet, Varennes, Québec, Canada, J3X 1S2

d : Department of Chemical and Biochemical Engineering, University of Western Ontario, London, Canada, N6A 5B9

Comments about:

"Is the rapid initial performance loss of Fe/N/C non precious metal catalysts due to micropore flooding?"
J. Y Choi, L. Yang, T. Kishimoto, X. Fu, S. Ye, Z. Chen and D. Banham
Energy Environ Sci., 2017, **10**, 296-305.

In this paper, Banham et al. criticized our previous hypothesis that micropore flooding was a major cause of the fast current decay of highly active and performing Fe/N/C electrocatalysts used at the cathode of PEM fuel cells.

This hypothesis was proposed in our previous paper:
"Is iron involved in the lack of stability of Fe/N/C electrocatalysts used to reduce oxygen at the cathode of PEM fuel cells?"
G. Zhang, R. Chenitz, M. Lefèvre, S. Sun, J. P. Dodelet
Nano Energy, 2016, **29**, 111-125.

In their paper, Banham et al. enumerate four possible mechanisms that have been mentioned in the literature and that could be possible mechanism to explain the rapid performance decay observed in most non-Platinum Metal Catalysts (NPMCs).

1. Demetalation of NMPCs [1-5]
2. Attack by H_2O_2 [6,7]and/or free radicals [8]
3. Protonation of the active sites [9]or protonation of a N species neighboring the active sites, followed by anion adsorption [10]
4. Micropore flooding [11 – 14].

The main body of their paper was used to demonstrate that micropore flooding has a minor contribution, if any, to the rapid performance loss during the first hours of stability test of their initially higly active and performing Fe/N/C catalyst in PEM fuel cell.
This conclusion was based on the following premices:
1. The total surface area of their catalyst was very high (1244 $m^2 g^{-1}$) with 1149 $m^2 g^{-1}$ of micropore and 94 $m^2 g^{-1}$ of mesopore surface areas.
2. Nafion ionomer could not enter in their micropores and the surface of the micropores had to be at least partially covered with a thin film of water, if not fully flooded initially to enable the diffusion of protons and of oxygen to the Fe-bearing active sites located in the micropores.
3. A double layer charging current was expected in the micropore during fuel cell operation. However, since no change in the double layer charging current was experimentally observed, this would suggest that the pores were in fact fully wetted initially.

The specific capacitance value measured for the catalytic layer was about 0.1 F m^{-2}.

From all these considerations, Banham et al. concluded that the majority of the surface area of the catalyst was fully accessed and initially wetted and that this surface area contributed to the catalyst double layer. Therefore an irreversible micropore flooding, occurring from a change of the catalyst surface from initially hydrophobic to hydrophilic upon oxidation of the catalyst, was not supported by their conclusions.

Today, we agree on this particular point that our previous hypothesis about the fast decrease of the current density of NC_Ar+NH$_3$, based on an irreversible micropore flooding, was wrong. We believe that the novel hypothesis that we give in our present work is much better. However, this novel hypothesis is based on *several premices that drastically differ from those used by Banham et al.*
1. The total surface are of NC_Ar+NH$_3$ is also very high (1185 m^2 g^{-1}) with 985m^2 g^{-1} of micropores and 200 m^2 g^{-1} of mesopores.
2. The micropores of our catalysts are open-end and slit-shaped. They are also interconnected in a micropore network which is initially hydrophobic.
3. Nafion ionomer cannot enter in the micropores of NC_Ar+NH$_3$ as well. However, contrary to Banham et al., water (and dissolved protons and O$_2$) quickly flows in these micropores entering as a stream of humidified air in a working cathode, if their width is ≥ 0.7 nm (this corresponds to 400 m^2 g^{-1} of micropore surface area), as water has no interaction with the micropore hydrophobic walls. This explains why Fe-N$_4$-like active sites located in the micropores are initially highly active and performing as they are fed with O$_2$ and protons that are dissolved in the flow of water running in these micropores. A strong participation to the initial current density cannot be rationalized by the simple diffusion of H$^+$ and O$_2$ in micropores.

Now, how is it possible to explain the rapid decay of the current density of NC_Ar+NH$_3$ or any similar Fe/N/C catalysts in fuel cell?

Banham et al. favor the oxidation of the carbon/active sites. According to their arguments, it is unlikely that carbon corrosion occurs electrochemically at a significant rate at potentials < 0.6V. Thus their leading hypothesis for the rapid performance decay of their catalyst is the chemical attack of carbon/active sites by H$_2$O$_2$ or by radicals.

We have already shown [13] that a reaction of the catalyst with H$_2$O$_2$ or •OH radicals (produced by the reaction of H$_2$O$_2$ with Fe^{2+} ions to obtain the Fenton reagent) is not important for NC_Ar+NH$_3$. A similar conclusion is expected to be drawn for the Fe/N/C catalyst of Banham et al. which is structurally close to NC_Ar+NH$_3$.

Our novel hypothesis is based on the chemical equilibrium of the demetalation reaction of FeN$_4$-like active sites located in the micropores. As any chemical reaction, this demetalation reaction is characterized by an equilibrium constant. Despite the relatively low possibility for these FeN$_4$-like sites to demetalate at equilibrium in the strong acid pH of the Nafion ionomer, the story is completely different when equilibrium is

never reached, as it is the case in the micropores. Indeed, in these conditions, any Fe ion released by the site will be quickly transported by the running water flux outside the micropore and Le Chatelier principle will apply, having the demetalation reaction running to completion in the micropores until all FeN_4-like sites in the micropores will be demetalated. This will drastically affect the initial current density.

Finally, we agree with the opinion of Banham et al when they declare at the end of their paper's conclusions that characterizing, understanding and overcoming the stability problem of highly active and performing ORR non-Platinum-metal (or generally speaking PGM-free) catalysts should be a large focus in the coming years within the PGM-free catalyst community.

References:
[1]   B. Wang, *Journal of Power Sources*, 2005, 152, 1-15.

[2]   D. Deng, L. Yu, X. Chen, G. Wang, L. Jin, X. Pan, J. Deng, G. Sun and X. Bao, *Angewandte Chemie International Edition*, 2013, **52**, 371-375.

[3]   C. H. Choi, C. Baldizzone, G. Polymeros, E. Pizzutilo, O. Kasian, A. K. Schuppert, N. Ranjbar Sahraie, M.-T. Sougrati, K. J. J. Mayrhofer and F. Jaouen, *ACS Catalysis*, 2016, **6**, 3136-3146.

[4]   J. A. Varnell, E. C. Tse, C. E. Schulz, T. T. Fister, R. T. Haasch, J. Timoshenko, A. I. Frenkel and A. A. Gewirth, *Nature Communications*, 2016, **7**, 12582.

[5]   C. H. Choi, C. Baldizzone, J.-P. Grote, A. K. Schuppert, F. Jaouen and K. J. J. Mayrhofer, *Angewandte Chemie International Edition*, 2015, **54**, 12753-12757

[6]   H. Schulenburg, S. Stankov, V. Schünemann, J. Radnik, I. Dorbandt, S. Fiechter, P. Bogdanoff and H. Tributsch, *The Journal of Physical Chemistry B*, 2003, **107**, 9034-9041.

[7]   V. Goellner, V. Armel, A. Zitolo, E. Fonda and F. Jaouen, *Journal of the Electrochemical Society*, 2015, **162**, H403-H414.

[8]   M. Lefèvre and J.-P. Dodelet, *Electrochimica Acta*, 2003, **48**, 2749-2760.

[9]   G. Liu, X. Li and B. Popov, *ECS Transactions, 2009*, **25**, 1251-1259.

[10]   J. Herranz, F. Jaouen, M. Lefèvre, U. I. Kramm, E. Proietti, J.-P. Dodelet, P. Bogdanoff, S. Fiechter, I. Abs- Wurmbach, P. Bertrand, T. M. Arruda and S. Mukerjee, *The Journal of Physical Chemistry C*, 2011, **115**, 16087-16097.

[11]   L. Yang, N. Larouche, R. Chenitz, G. Zhang, M. Lefèvre and J.-P. Dodelet, *Electrochimica Acta*, 2015, **159**, 184-197.

[12]   Y.-C. Wang, Y.-J. Lai, L. Song, Z.-Y. Zhou, J.-G. Liu, Q. Wang, X.- D. Yang, C. Chen, W. Shi, Y.-P. Zheng, M. Rauf and S.-G. Sun, *Angewandte Chemie International Edition*, 2015, **54**, 9907- 9910.

[13]   G. Zhang, R. Chenitz, M. Lefèvre, S. Sun and J.-P. Dodelet, *Nano Energy*, 2016,**29**, 111-129.

[14]   M. Shao, Q. Chang, J. P. Dodelet and R. Chenitz, *Chem. Rev.*, 2016, **116**, 3594-3657.

Supplementary Information : Figures

A specific demetalation of Fe-N$_4$ catalytic sites in the micropores of NC_Ar+NH$_3$ is at the origin of the initial activity loss of this highly active Fe/N/C catalyst used for the reduction of oxygen in PEM fuel cells

Régis Chenitz[a], Ulrike Kramm[b], Michel Lefèvre[c], Vassili Glibin[d], Gaixia Zhang[a], Shuhui Sun[a], Jean-Pol Dodelet[a,*]

a : INRS-Énergie, Matériaux et Télécommunications, 1650 Boulevard Lionel Boulet, Varennes, Québec, Canada,   J3X 1S2

b : TU Darmstadt, Graduate School of Excellence Energy Science and Engineering, Otto-Berndt-Str. 3, 64287 Darmstadt, Germany

c : Canetique Electrocatalysis, 1650 Boulevard Lionel Boulet, Varennes, Québec, Canada, J3X 1S2

d : Department of Chemical and Biochemical Engineering, University of Western Ontario, London, Canada,
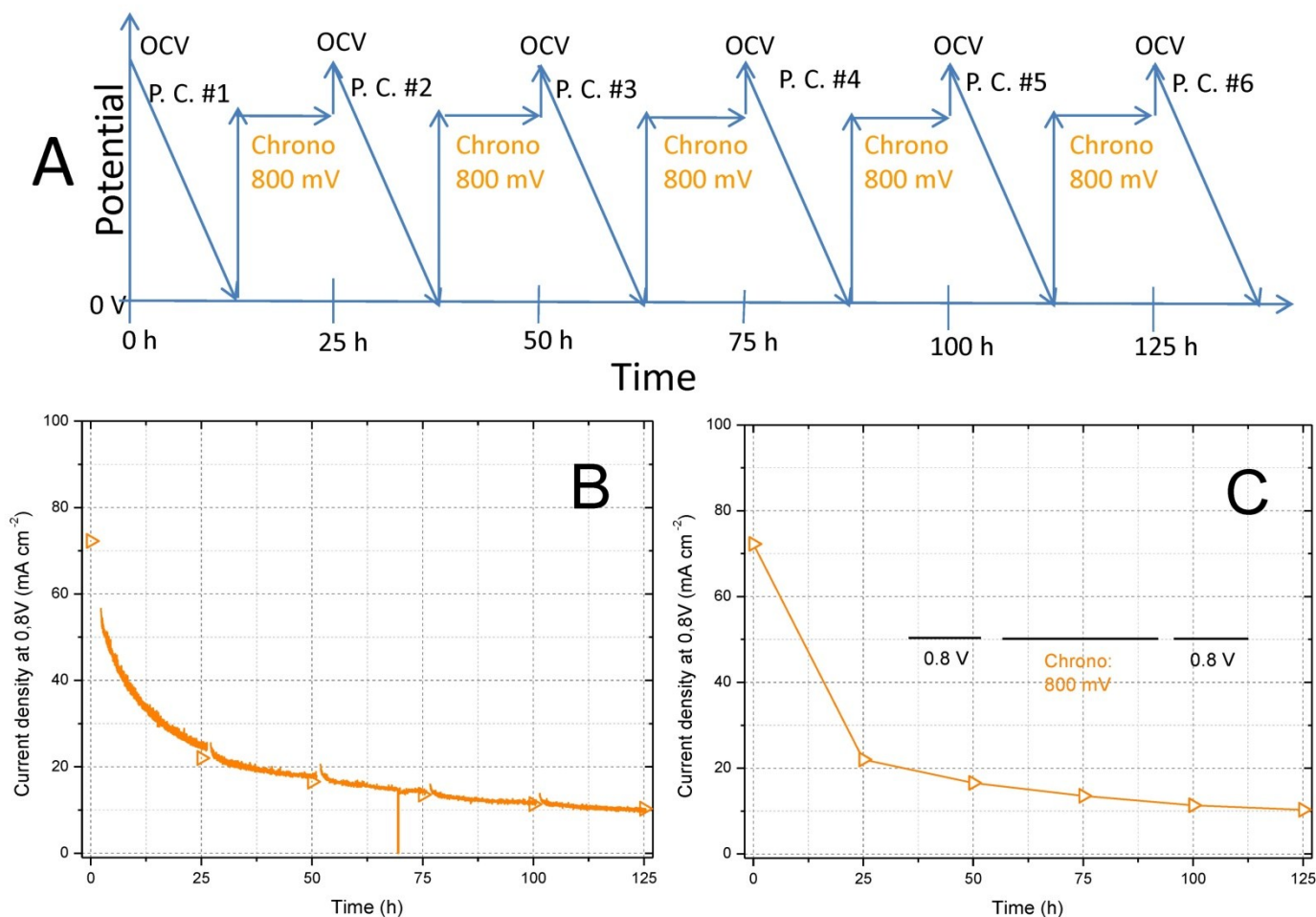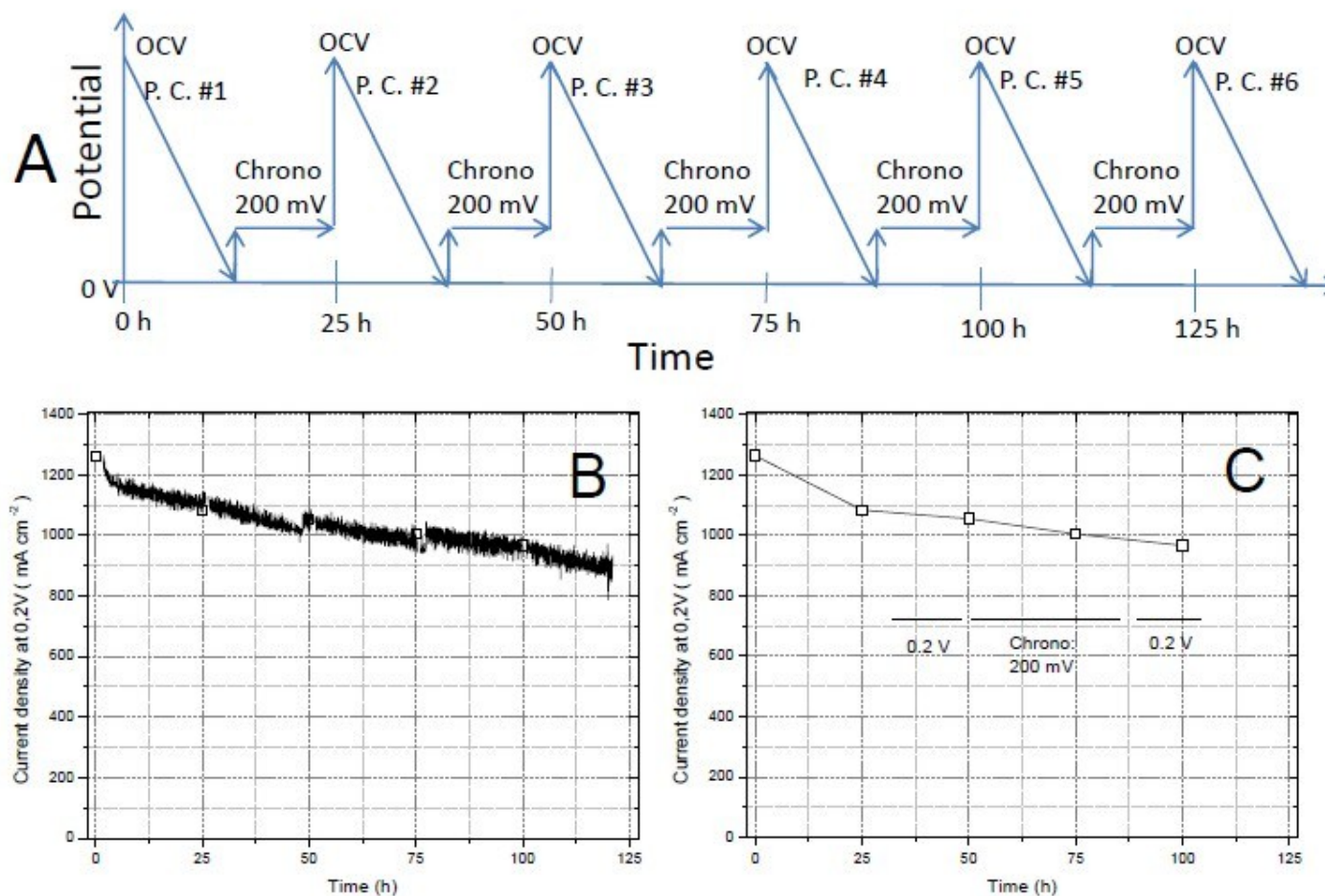
Figure S1: (A) Sequence of experiments for MEA#2 analyzed by recording polarization curves (P.C.) at a sweep rate of 0.5 mV s^{-1} in alternation with chrono-amperometries at 800 mV; (B) Change in current density measured at 0.8V during the five chrono-amperometry segments recorded at 800 mV and lasting 25h each; the symbols are current density values read at 0.8V on each of the six polarization curves recorded during the entire 125h catalyst durability experiment; (C) same symbols than in -B- but with joining lines
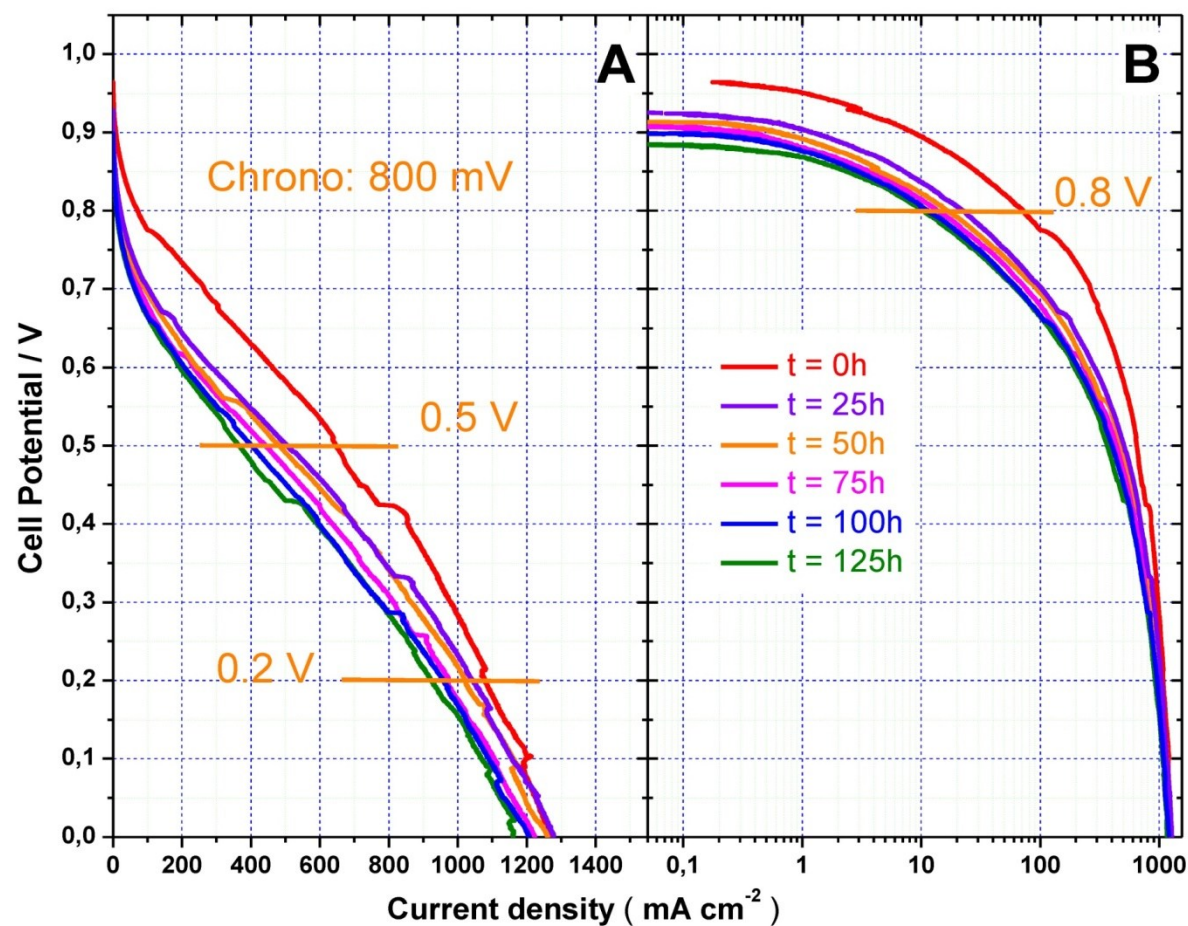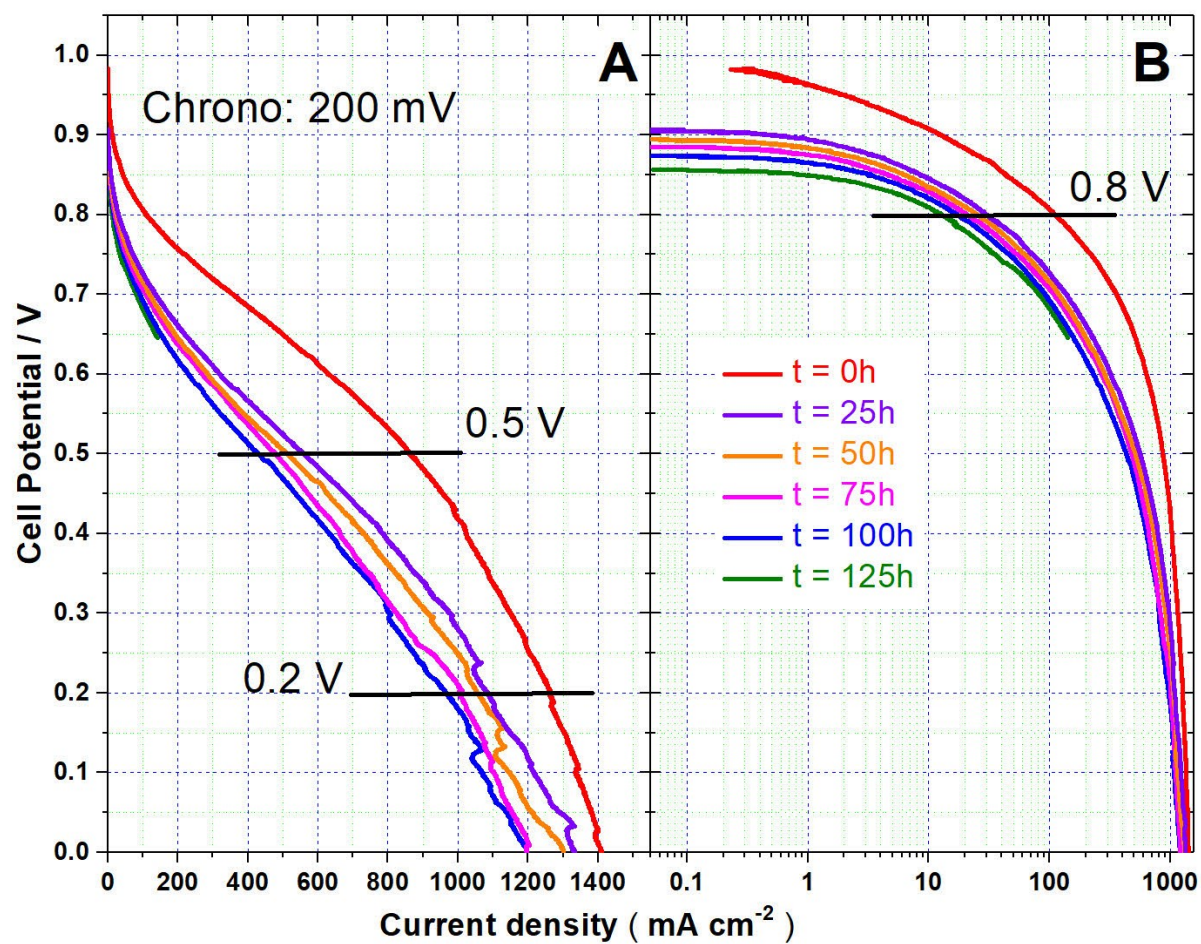
Figure S2: (A) Classical and (B) Tafel representations of the six polarization curves for MEA#2 recorded initially (t = 0h) and after each of the five chrono-amperometry segment of 25h at 800 mV. The change in current density with elapsed time for MEA#2 is probed by horizontal lines at three potentials: 0.8, 0.5, and 0.2V
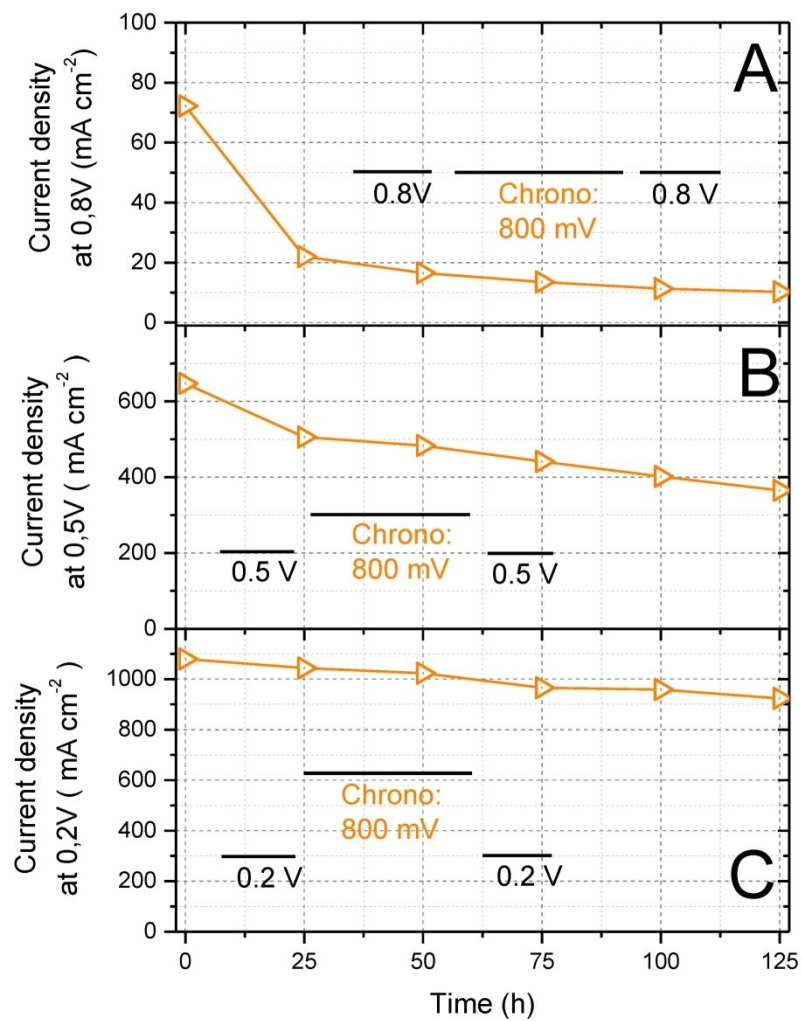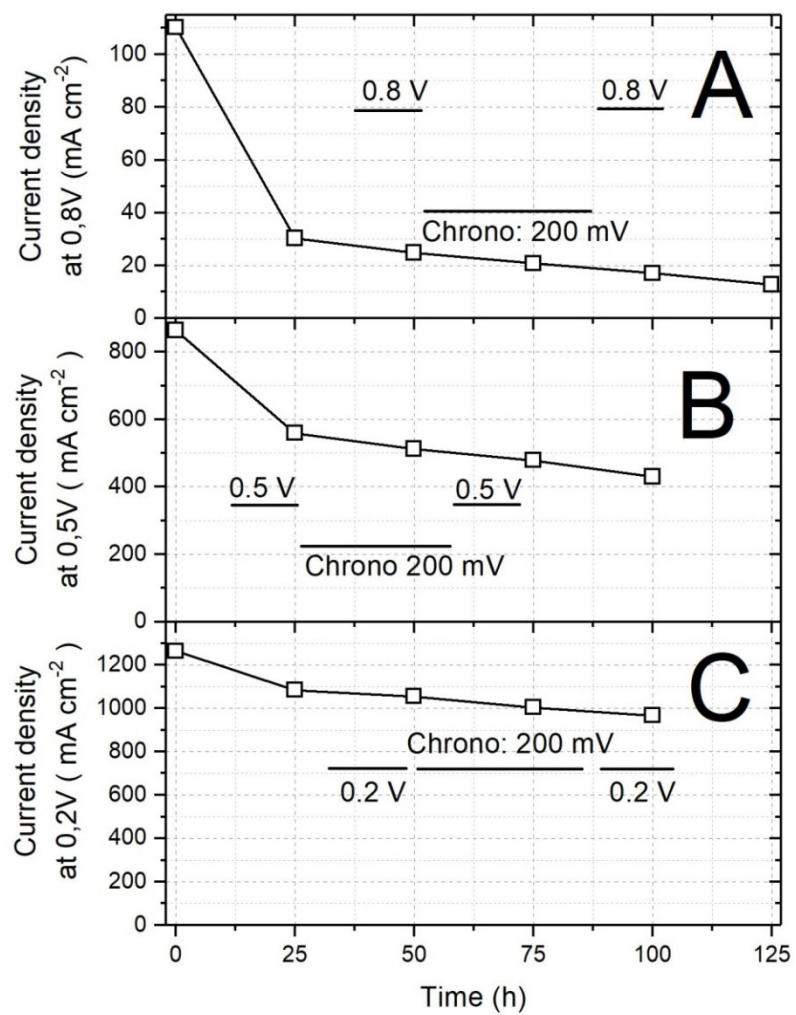
Figure S3: Punctual evolution at 0.8V (A), 0.5V (B), and 0.2V (C) of the current density read for MEA#2 on the sequence of polarization curves recorded at t = 0h and after each of the five chrono-amperometry segments of 25h at 800 mV.

Figure S4: (A) Sequence of experiments for MEA#3 analyzed by recording polarization curves (P.C.) at a sweep rate of 0.5 mV s^{-1} in alternation with chrono-amperometries at 200 mV; (B) Change in current density measured at 0.2V during the five chrono-amperometry segments recorded at 200 mV and lasting 25h each; the symbols are current density values read at 0.2V on each of the six polarization curves recorded during the entire 125h catalyst durability experiment; (C) same symbols than in -B- but with joining lines.

10

Figure S5: (A) Classical and (B) Tafel representations of the six polarization curves for MEA#3 recorded initially (t = 0h) and after each of the five chrono-amperometry segment of 25h at 200 mV. The change in current density with elapsed time for MEA#3 is probed by horizontal lines at three potentials: 0.8, 0.5, and 0.2V.

Figure S6: Punctual evolution at 0.8V (A), 0.5V (B), and 0.2V (C) of the current density read for MEA#3 on the sequence of polarization curves recorded at t = 0h and after each of the five chrono-amperometry segments of 25h at 200 mV.
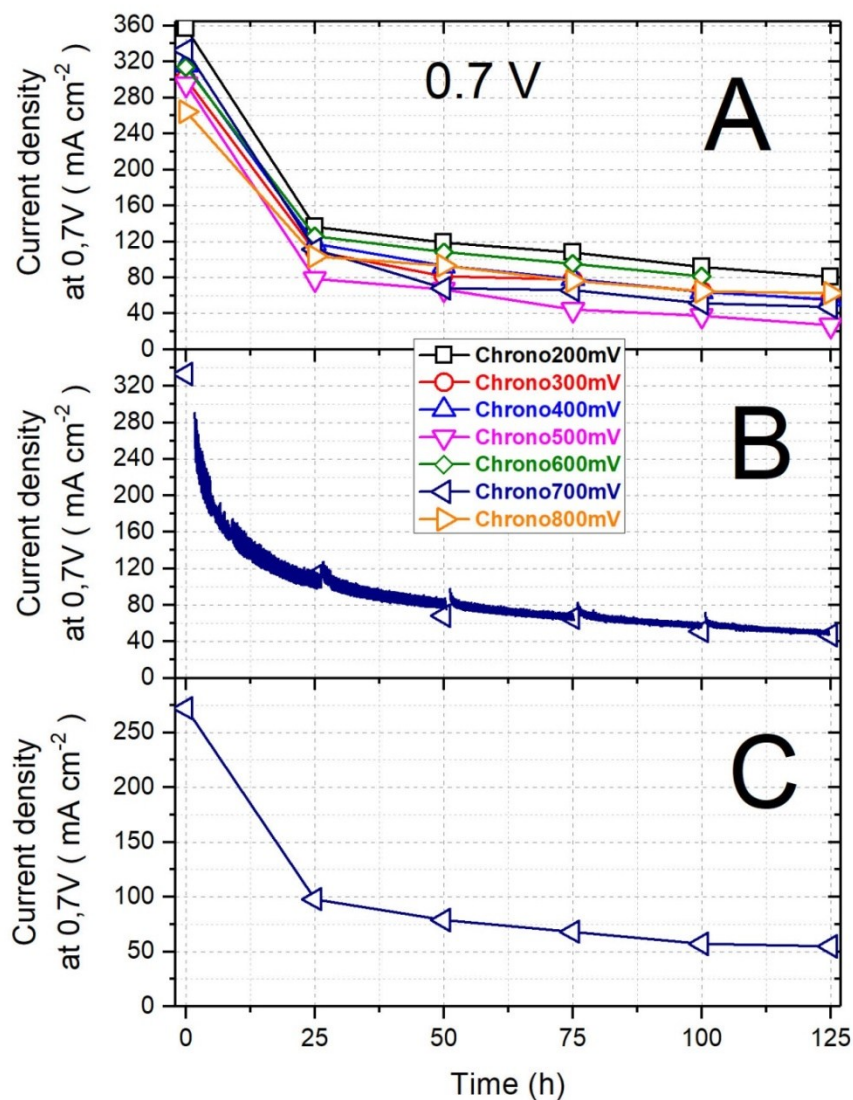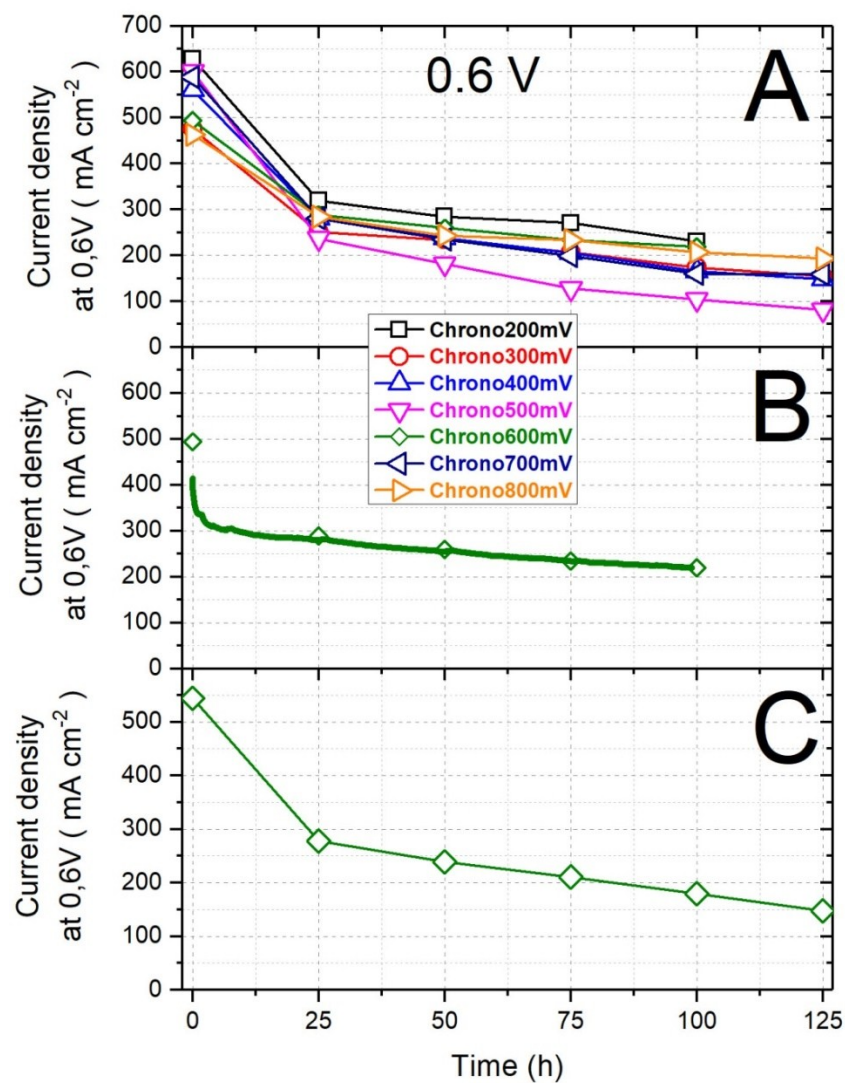
Figure S7: (A) Current density values read at 0.7V on each of the six polarization curves recorded during the entire 125h experiment for all seven MEAs used in this work, each MEA having been maintained at a different chrono-amperometric potential (between 200 to 800 mV) during the stability experiment; (B)Change in current density at 0.7V during the five 25h chrono-amperometry segments at 700 mV; the symbols are the current density values read at 0.7V on each polarization curve; (C) average current density values of Figure S7A at t = 0h and after 25, 50, 75, 100, and 125h for all seven MEAs used in this work, each MEA having been maintained at a different potential (from 200 to 800 mV) during the stability experiment
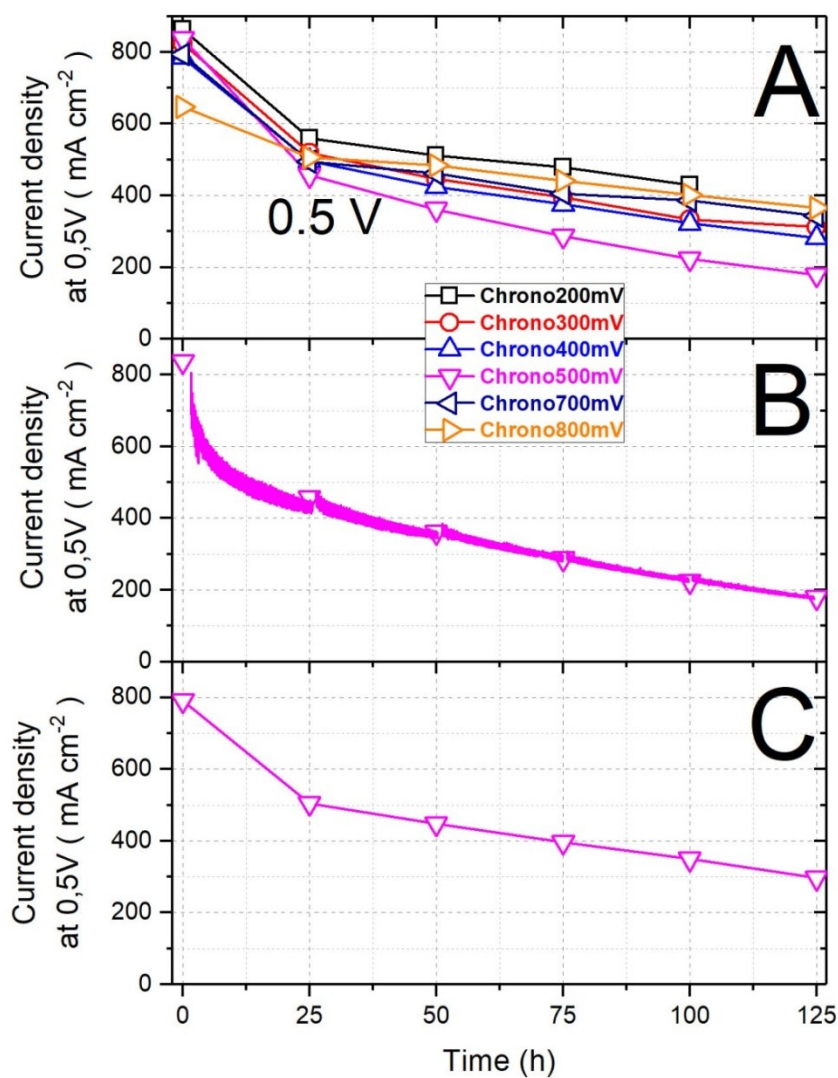
Figure S8: (A) Current density values read at 0.6V on each of the six polarization curves recorded during the entire 125h experiment for all seven MEAs used in this work, each MEA having been maintained at a different chrono-amperometric potential (between 200 to 800 mV) during the stability experiment; (B)Change in current density at 0.6V during the five 25h chrono-amperometry segments at 600 mV; the symbols are the current density values read at 0.6V on each polarization curve; (C) average current density values of Figure S8A at t = 0h and after 25, 50, 75, 100, and 125h for all seven MEAs used in this work, each MEA having been maintained at a different potential (from 200 to 800 mV) during the stability experiment
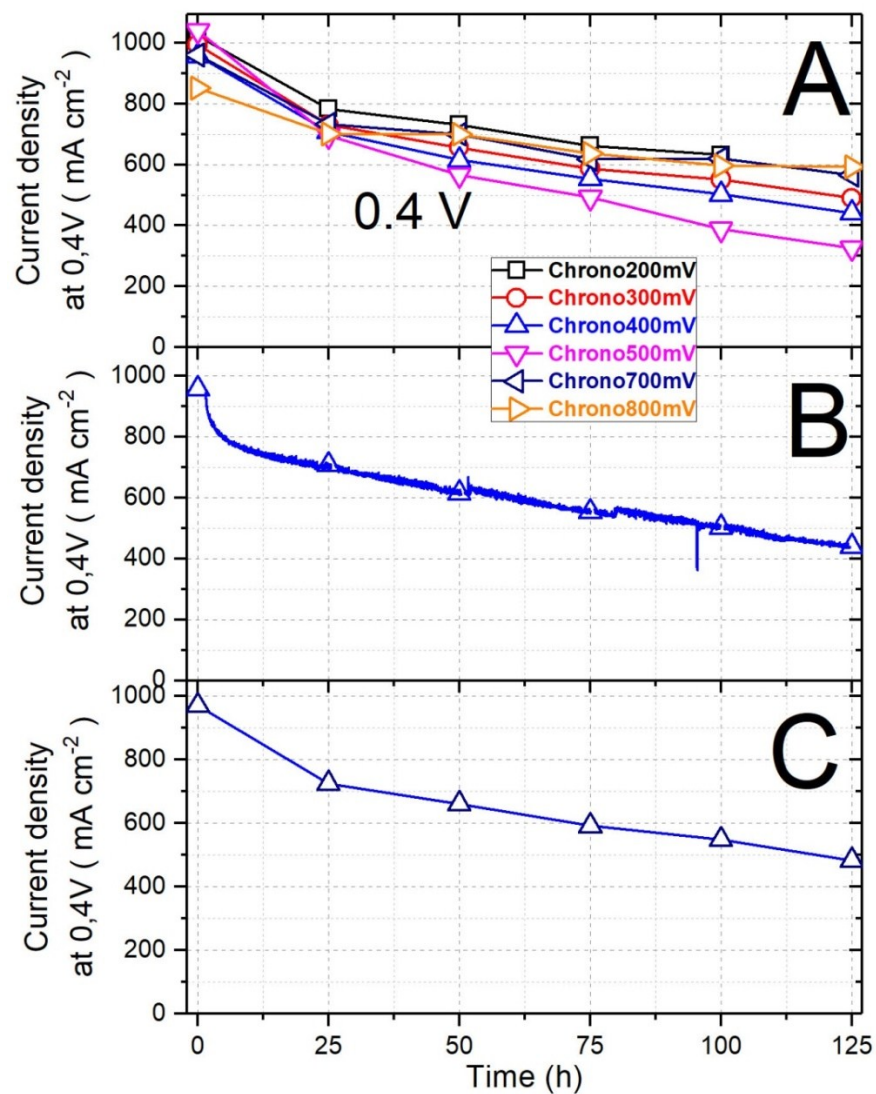
Figure S9: (A) Current density values read at 0.5V on each of the six polarization curves recorded during the entire 125h experiment for all seven MEAs used in this work, each MEA having been maintained at a different chrono-amperometric potential (between 200 to 800 mV) during the stability experiment; (B)Change in current density at 0.5V during the five 25h chrono-amperometry segments at 500 mV; the symbols are the current density values read at 0.5V on each polarization curve; (C) average current density values of Figure S9A at t = 0h and after 25, 50, 75, 100, and 125h for all seven MEAs used in this work, each MEA having been maintained at a different potential (from 200 to 800 mV) during the stability experiment
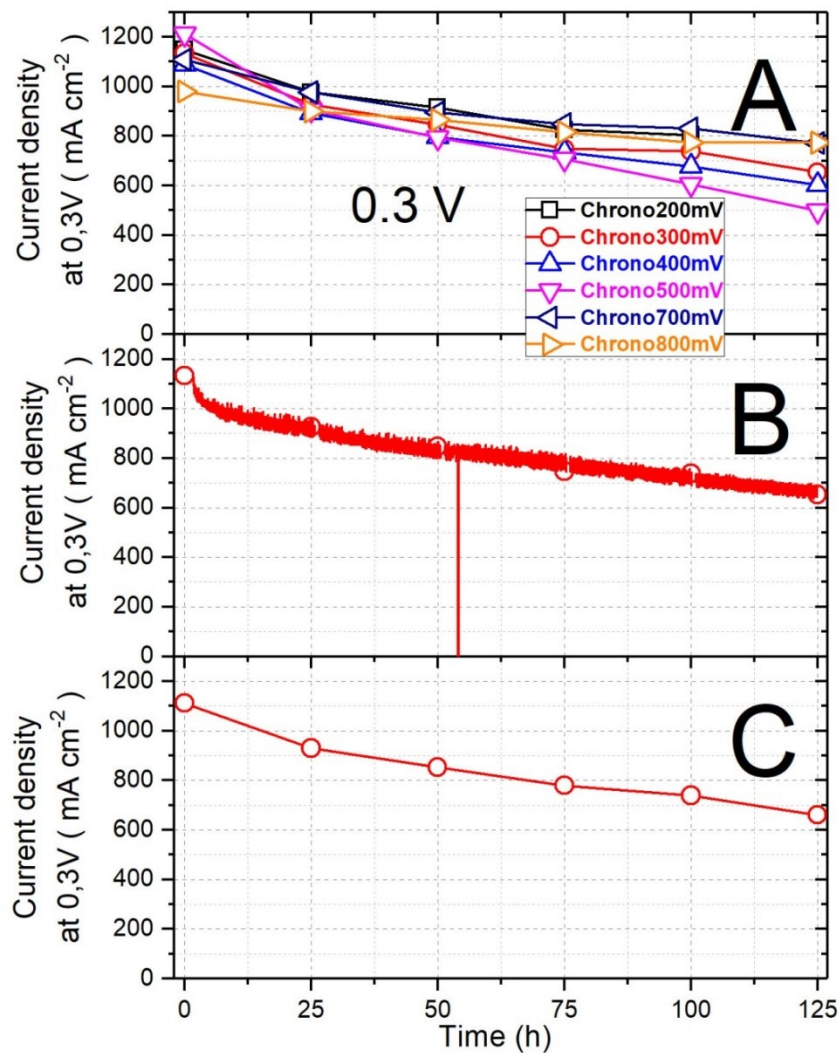
Figure S10: (A) Current density values read at 0.4V on each of the six polarization curves recorded during the entire 125h experiment for all seven MEAs used in this work, each MEA having been maintained at a different chrono-amperometric potential (between 200 to 800 mV) during the stability experiment; (B)Change in current density at 0.4V during the five 25h chrono-amperometry segments at 400 mV; the symbols are the current density values read at 0.4V on each polarization curve; (C) average current density values of Figure S10A at t = 0h and after 25, 50, 75, 100, and 125h for all seven MEAs used in this work, each MEA having been maintained at a different potential (from 200 to 800 mV) during the stability experiment

Figure S11: (A) Current density values read at 0.3V on each of the six polarization curves recorded during the entire 125h experiment for all seven MEAs used in this work, each MEA having been maintained at a different chrono-amperometric potential (between 200 to 800 mV) during the stability experiment; (B)Change in current density at 0.3V during the five 25h chrono-amperometry segments at 300 mV; the symbols are the current density values read at 0.3V on each polarization curve; (C) average current density values of Figure S11A at t = 0h and after 25, 50, 75, 100, and 125h for all seven MEAs used in this work, each MEA having been maintained at a different potential (from 200 to 800 mV) during the stability experiment
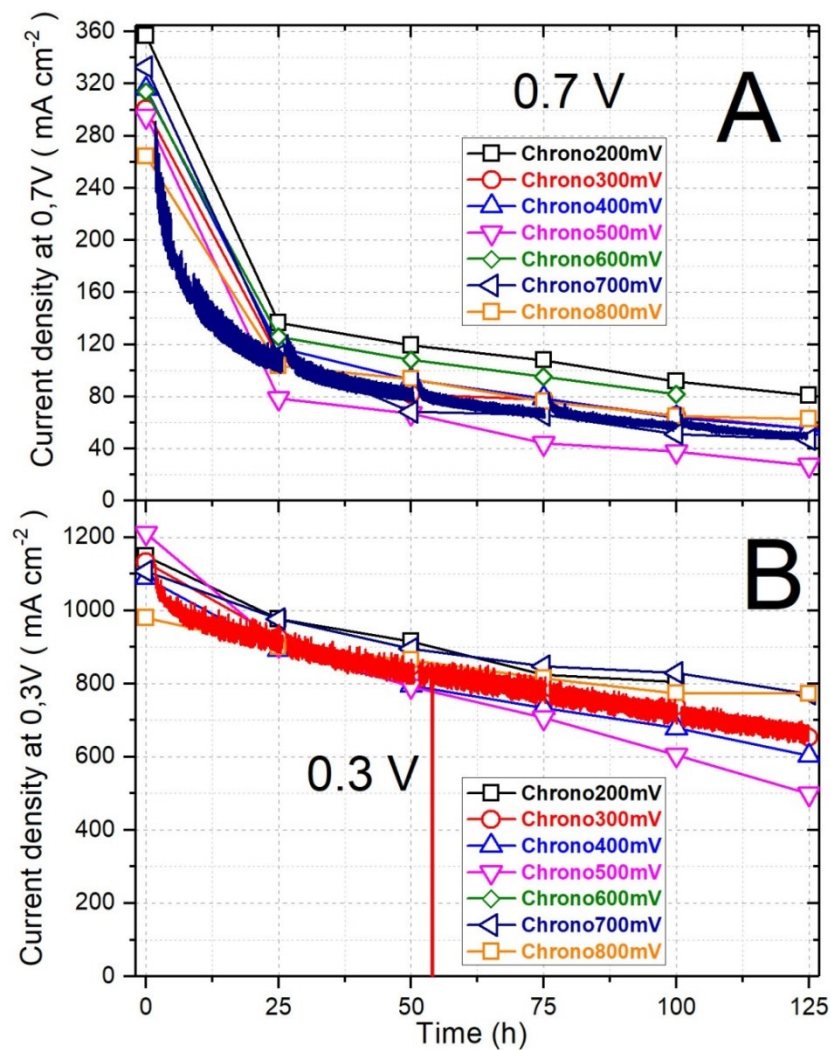
Figure S12: **Superposition of (i)** the current density values read at 0.7V (A) or 0.3V (B) on each of the six polarization curves recorded during the entire 125h experiment for all seven MEAs used in this work, each MEA having been maintained at a different chrono-amperometric potential (from 200 to 800 mV) during the stability experiment; **and (ii)** the change in current density at 0.7V (A) and 0.3V (B) during the five 25h chrono-amperometric segments at either 700 mV (A) or 300 mV (B).
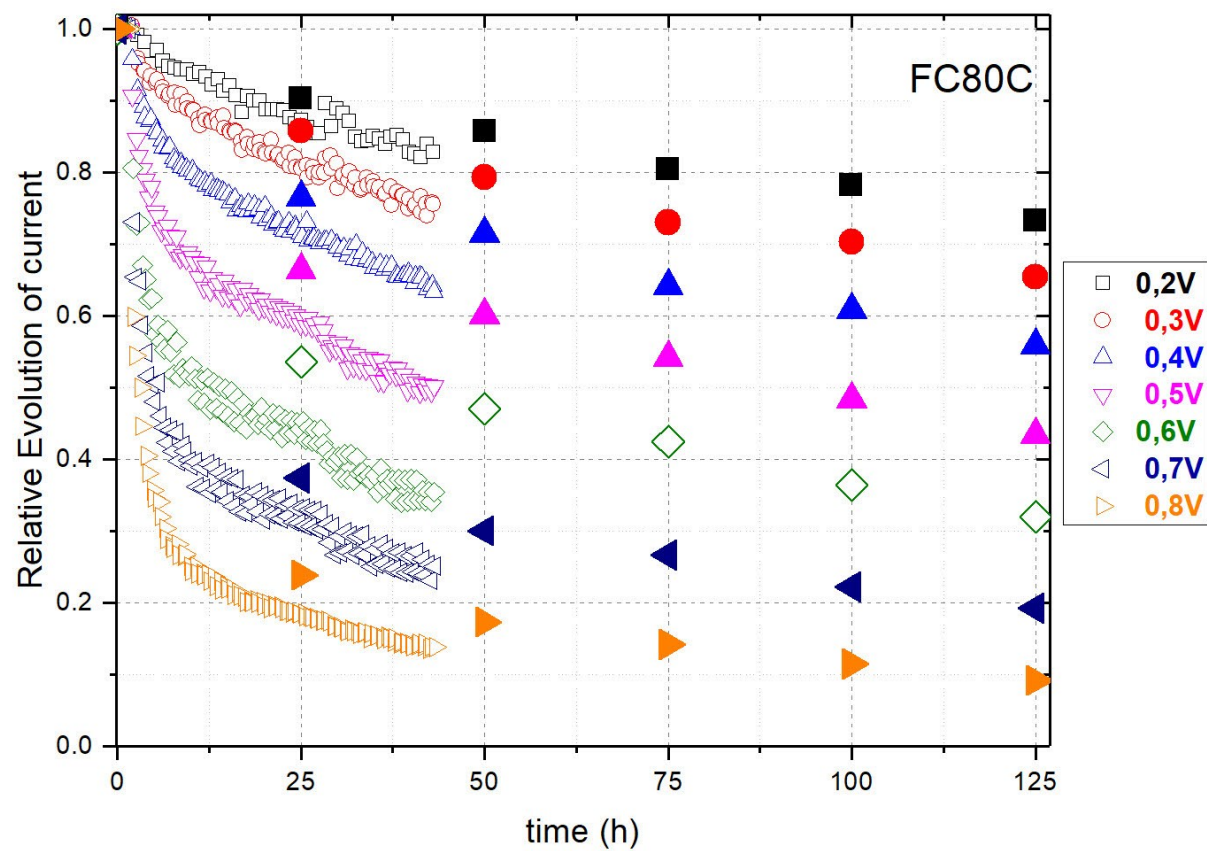
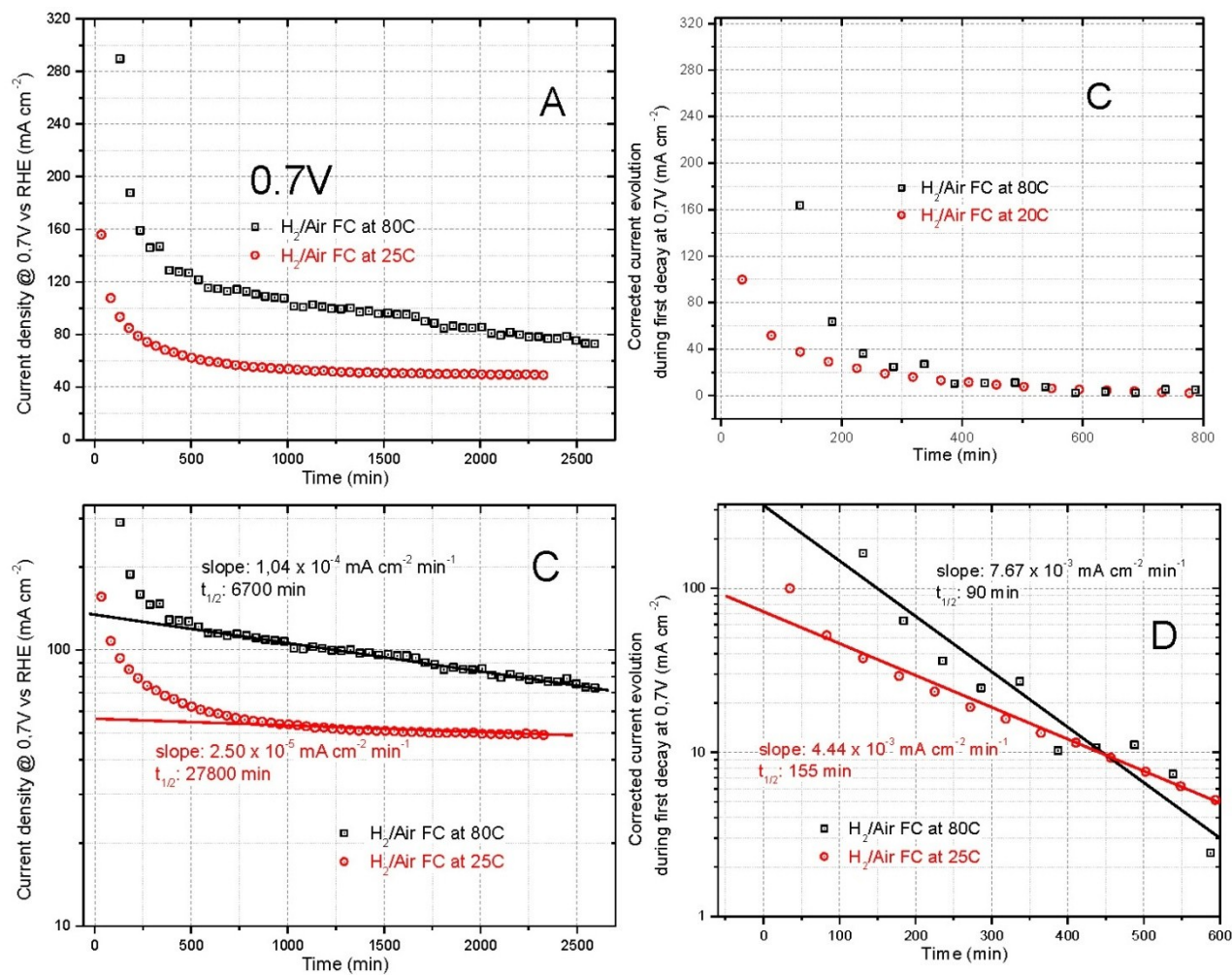Figure S13: Comparison between Figure 6A and Figure 7A for fuel cells working at 80°C

Figure S14: (A) Time evolution of current densities in zones 1 and 2 at 0.7V in H_2/air PEM fuel cell and at

80^oC (black symbols) and 25^oC (red symbols); (B) Half-life determination for the exponential decay of the current density in zone 2; (C) Exponential decay of the current density in zone 1 (D) Half-life determination for the exponential decay in zone 1.
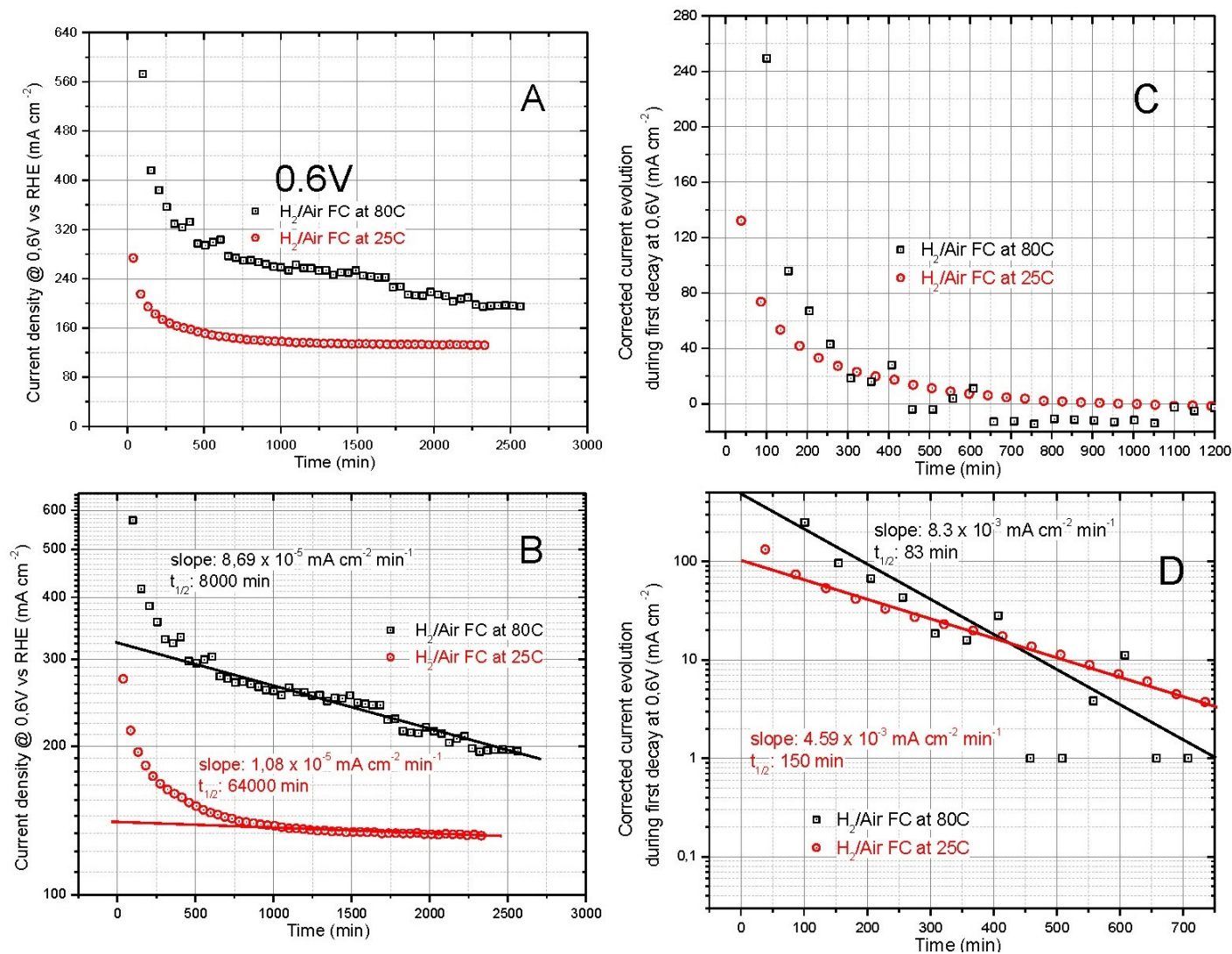
Figure S15: (A) Time evolution of current densities in zones 1 and 2 at 0.6V in H_2/air PEM fuel cell and at

80°C (black symbols) and 25°C (red symbols); (B) Half-life determination for the exponential decay of the current density in zone 2; (C) Exponential decay of the current density in zone 1 (D) Half-life determination for the exponential decay in zone 1.
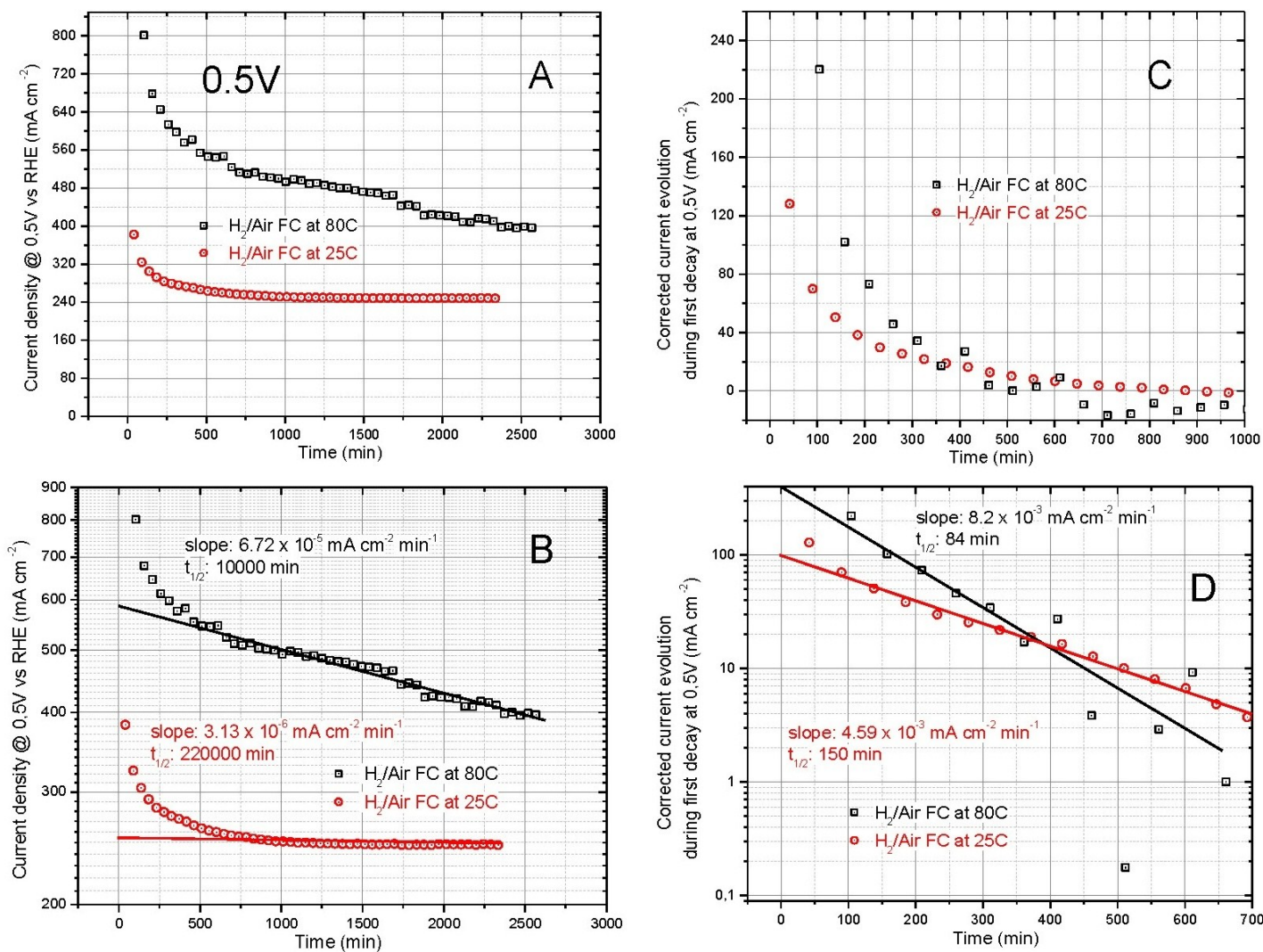
Figure S16: (A) Time evolution of current densities in zones 1 and 2 at 0.5V in H_2/air PEM fuel cell and at 80°C (black symbols) and 25°C (red symbols); (B) Half-life determination for the exponential decay of the current density in zone 2; (C) Exponential decay of the current density in zone 1 (D) Half-life determination for the exponential decay in zone 1.
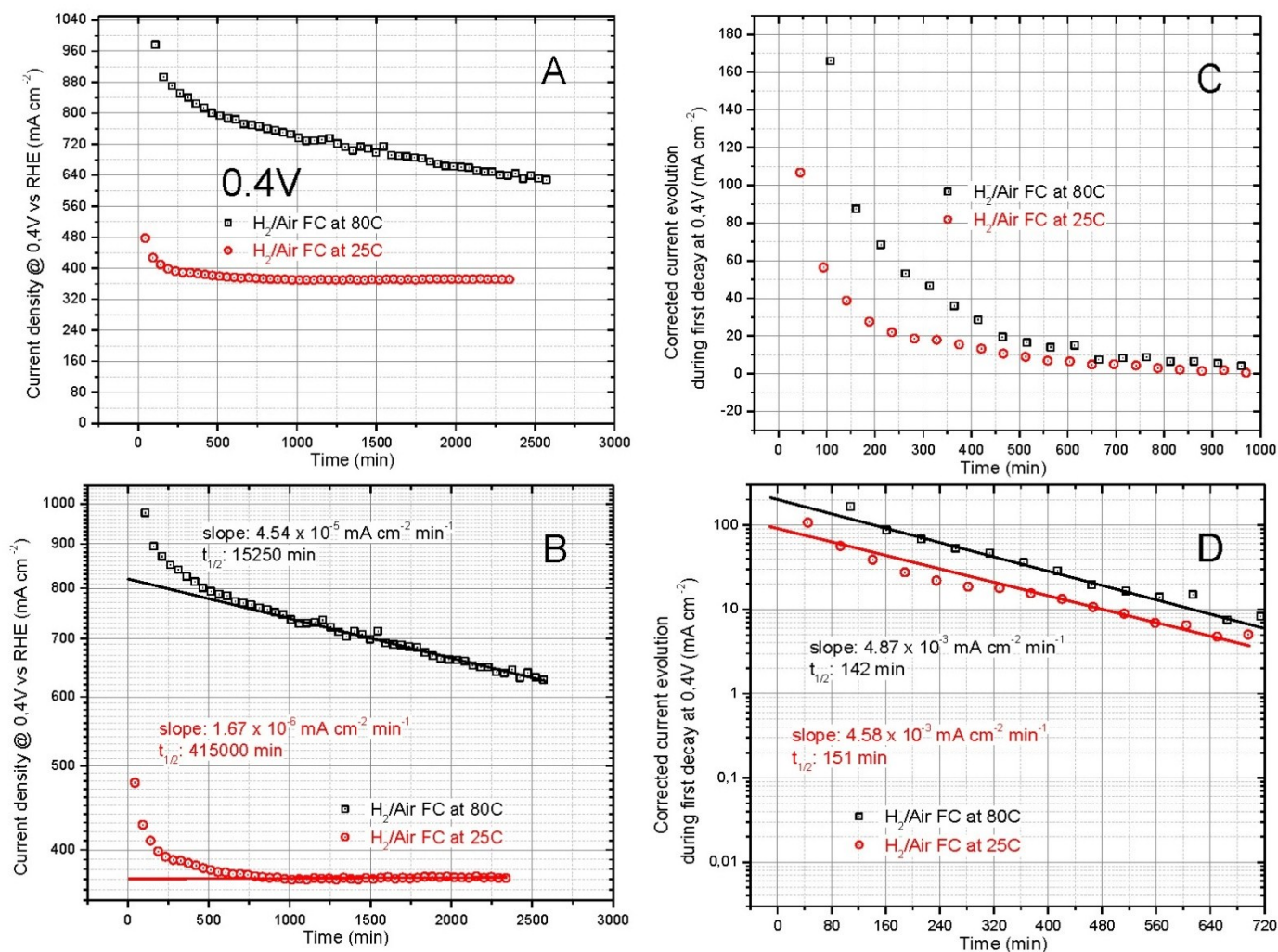
Figure S17: (A) Time evolution of current densities in zones 1 and 2 at 0.4V in H_2/air PEM fuel cell and at 80°C (black symbols) and 25°C (red symbols); (B) Half-life determination for the exponential decay of the current density in zone 2; (C) Exponential decay of the current density in zone 1 (D) Half-life determination for the exponential decay in zone 1.
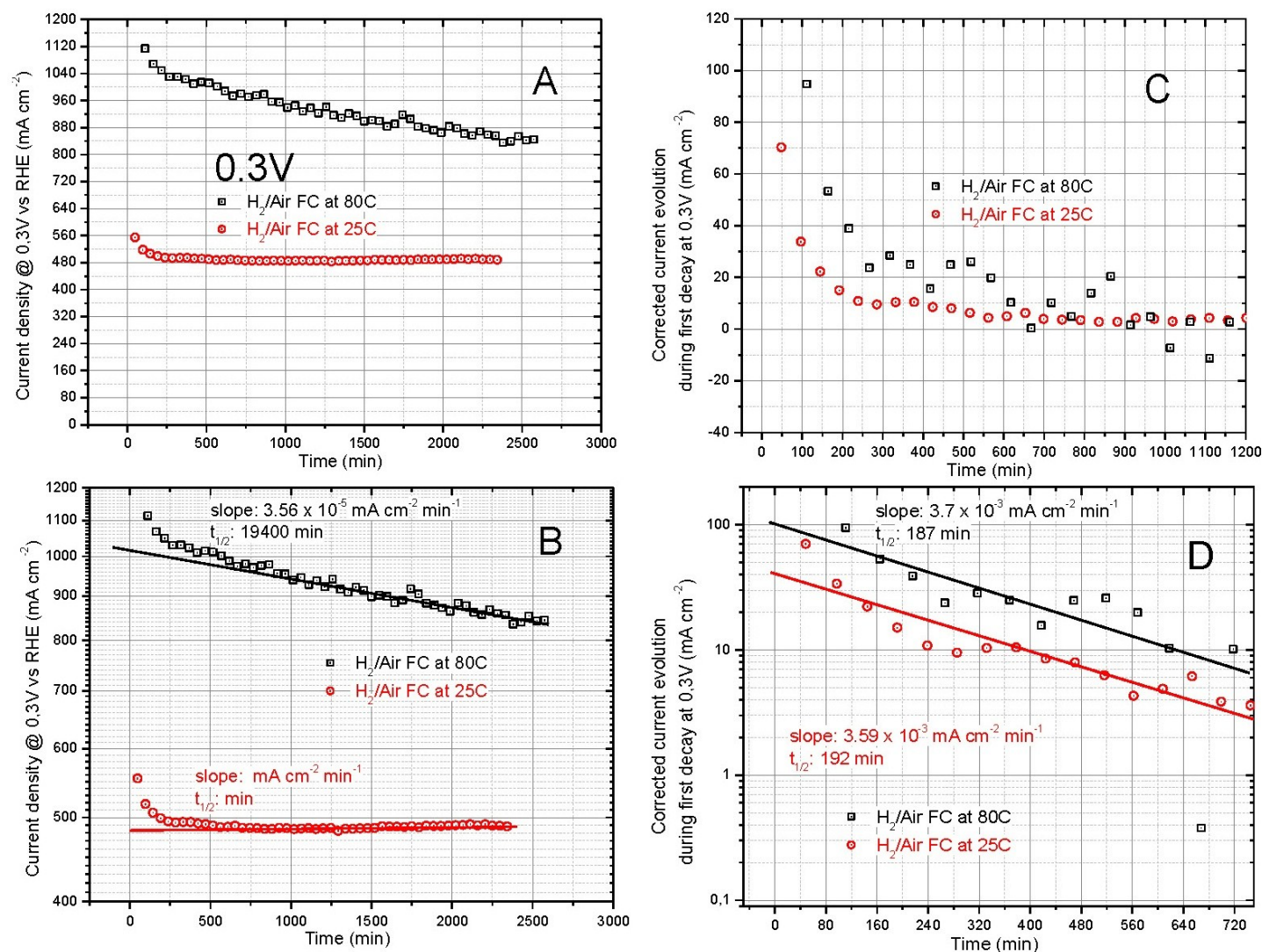
Figure S18: (A) Time evolution of current densities in zones 1 and 2 at 0.3V in H_2/air PEM fuel cell and at 80°C (black symbols) and 25°C (red symbols); (B) Half-life determination for the exponential decay of the current density in zone 2; (C) Exponential decay of the current density in zone 1 (D) Half-life determination for the exponential decay in zone 1
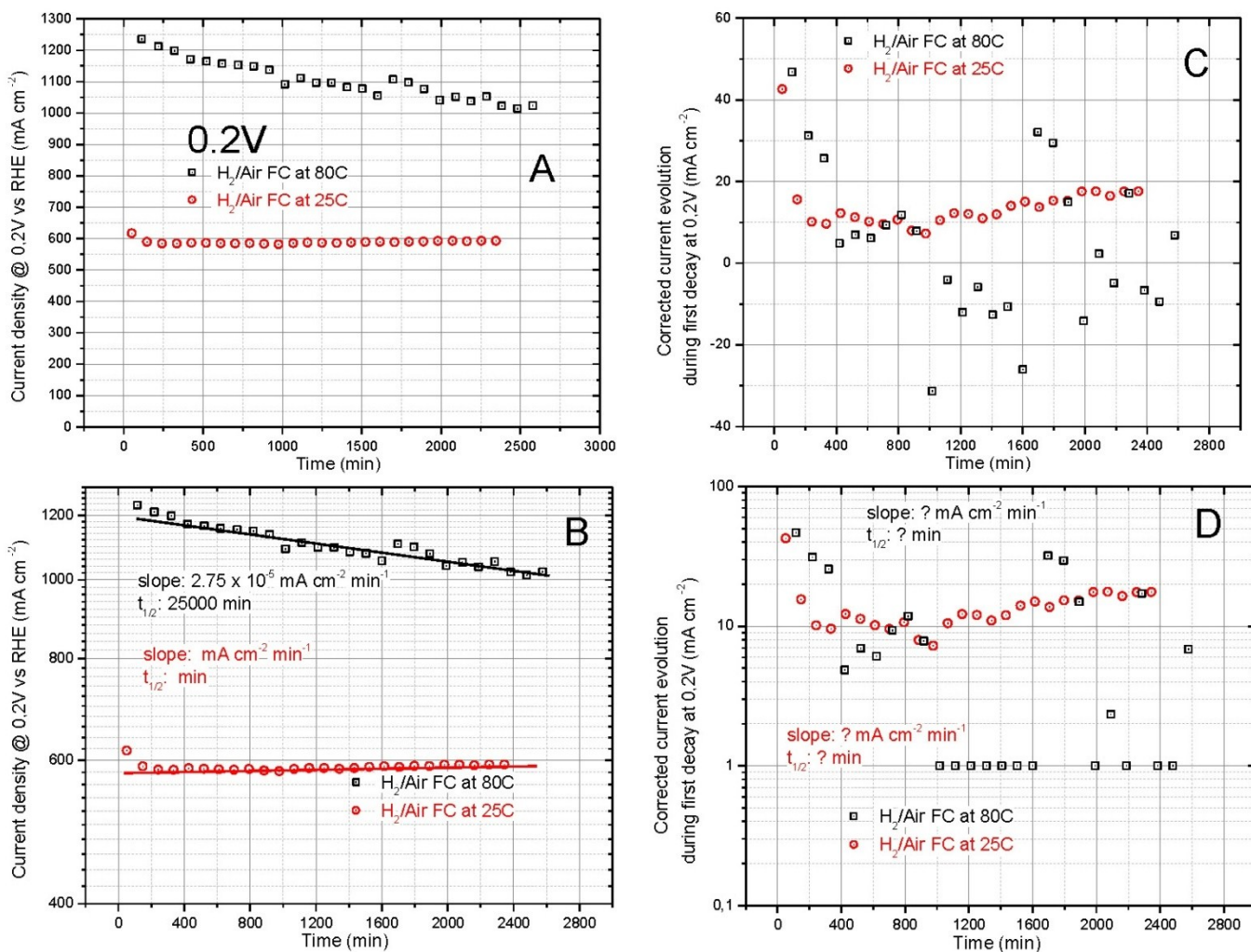
24

Figure S19: (A) Time evolution of current densities in zones 1 and 2 at 0.2V in H_2/air PEM fuel cell and at 80°C (black symbols) and 25°C (red symbols); (B) Half-life determination for the exponential decay of the current density in zone 2; (C) Exponential decay of the current density in zone 1 (D) Half-life determination for the exponential decay in zone 1.
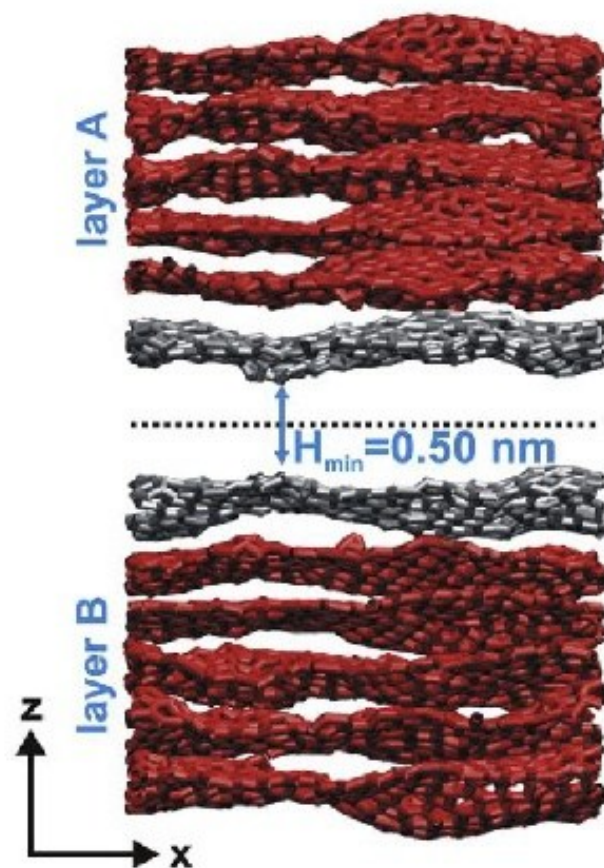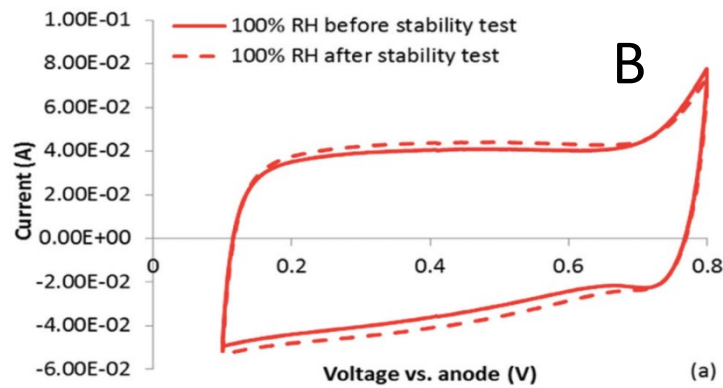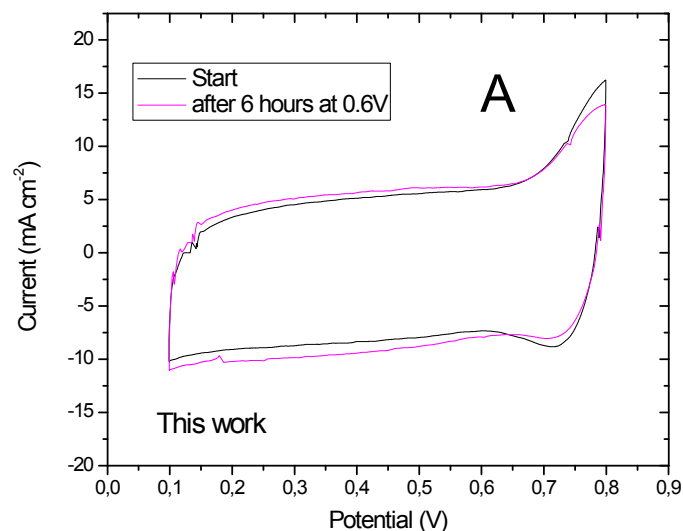
Figure S20: Slit-shaped pore in morphologically disordered LMA10 model carbon [Figure 2 from Ref. [60] in the main text], showing as well intra-wall ultramicropores (pores < 0.7 nm) also accessible to N_2 molecules during adsorption measurements. The ultramicropores are generated at the carbon surface by the protruding graphene sheets.

Figure S21 : (A) CVs in H_2/N_2 (Start) and after a 6h stability test at constant potential of 0.6V in H_2/Air; (B) CVs before and after 4h stability test at constant potential of 0.4V in H_2/Air published in Ref. **[1].**

H_2/N_2 or H_2/Air, 15 psig back-pressure, 0.3 lpm 100% humidified.

NC_Ar+NH₃ loading: 4.0 mg cm⁻². Fuel cell size: 1.14 cm².

Ratio 1.25 Nafion/Catalyst (Nafion 56 wt% and Catalyst 44 wt%)
NRE-211 membrane.

Fuel cell temperature: 80°C

H_2/N_2 or H_2/Air, 15 psig back-pressure, 0.2 lpm 100% humidified.

Fe-N-C-PANI-Phen catalyst loading: 3.8 mgcm⁻². Fuel cell size: 5 cm².
Nafion 35 wt% and Catalyst 65 wt%.
NRE211 membrane.

Fuel cell temperature: 80°C.

The similarity between: (i - Fig. S21 (A)) the CVs in H_2/N_2 of NC_Ar+NH₃ (Start) and after 6h stability test at constant potential at 0.6V in H_2/Air in and (ii - Fig. 21 (B)) the CVs in H_2/N_2 of Fe-N-C-PANI-Phen (before and after 4h stability test at constant potential at 0.4V in H_2/Air), is striking. The result from Banham et al. **[1]** was used to conclude that micropore flooding that was proposed in **[2]** to occur after electro-oxidation of the surface of the catalyst was not the cause of the rapid initial performance loss of NC_Ar+NH₃. Even if, in the present work, we used a higher potential (0.6V) and a longer stability test (6h) for which more electro-oxidation of the surface of NC_Ar+NH₃ would be expected than for the work of Banham et al recorded at 0.4V after 4h stability test, the similarity of Figures A and B enables us to reach in section R3.2 of the main text to the same conclusion than Banham et al.: the electro-oxidation of the surface of the catalyst is not the main cause of the rapid initial performance loss of NC_Ar+NH₃.

[2] G. Zhang, R. Chenitz, M. Lefèvre, S. Sun, J. P. Dodelet, *Nano Energy*, 2016, **29**, 111-125.
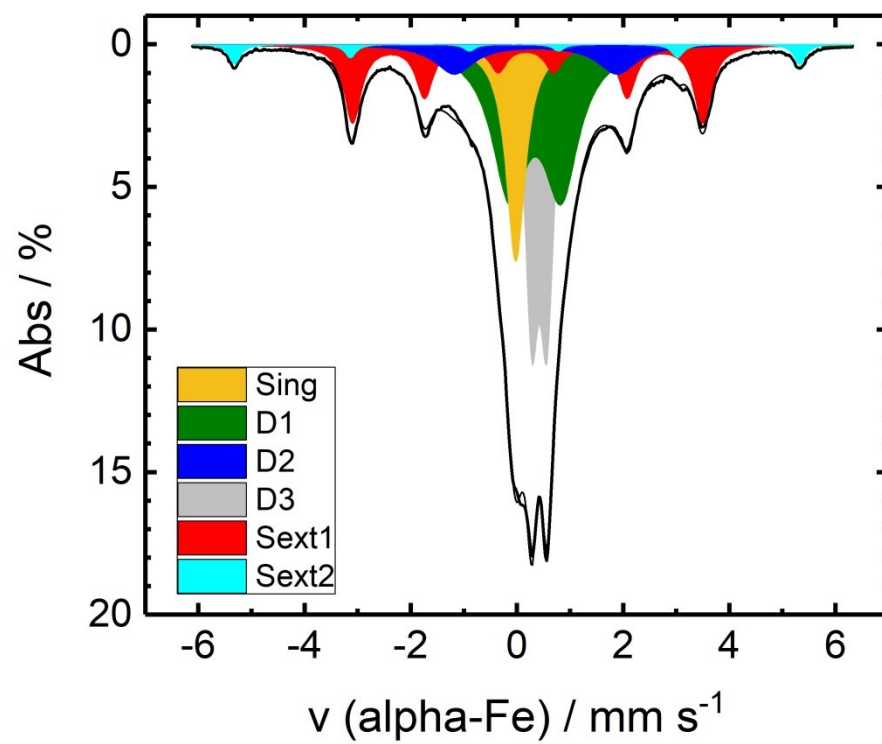
Figure S22: MEA prepared with NC_Ar+NH$_3$ before subjecting it to any fuel cell testing (t = 0h) and used as reference (100%) in Figure 12 of the main text.

Table S1 summarizing the Mössbauer parameters and assignments of iron species

	δ_{iso}	ΔE_Q	fwhm	H_0	Area	Assignments
	/ mm s^{-1}			/ T	/ %^{a}	
Sing	-0.02	-	0.44	-	14.1	Superparamagnetic iron
D1	0.35	0.98	0.8	-	33.3	« Organic » FeN_4, site 1
D2	0.36	3.06	0.9	-	7.8	« Organic » FeN_4, site 2
D3	0.42	0.28	0.30	-	23.6	Iron nitride Fe_xN (x ≤ 2.1)
Sext1	0.19	0.02	0.39	20.4	18.2	Iron carbide
Sext2	-0.02	0.03	0.26	33.0	3.1	Alpha iron

a: The iron content in the MEA is 0.47 wt%

- The "organic iron species" are responsible for the entire ORR current density produced by NC_Ar+NH$_3$.
- D3 has been identified by XRD as FexN with (x ≤ 2.1) in a previous work [1].
  Although some transition nitrides like MoN, Mo$_2$N, TiN, etc… display some ORR activity in acid medium or in fuel cell [2], iron nitride is not known to display ORR activity. As a matter of fact, a recent publication [3] and previous publication by one of us [4-6] have shown that FeN$_4$ sites have a far superior ORR activity in acid medium compared with Fe$_2$N or Fe$_3$C.
- As far as superparamagnetic and alpha iron particles are concerned, they are both prone to become iron ions in the strongly acid medium of Nafion, if they are not protected from dissolution by some carbonaceous or graphitic layers.

[1]   U. I. Kramm, J. Herranz, N. Larouche, T. M. Arruda, M. Lefèvre, F. Jaouen, P. Bogdanoff, S. Fiechter, I. Abs-Wurmbach, S. Mukerjee, J. P. Dodelet, *Phys. Chem. Chem. Phys.* 2012, **14**, 11673-11688.
[2]   S. Dong, X. Chen, X. Zhang, G. Cui, *Coordination Chemistry Reviews* 2013, **257**, 1946-1956.
[3]   T. Sun, Y. Jiang, Q. Wu, L. Du, Z. Zhang, L. Yang, X. Wang, Z. Hu, *Catal. Sci. Technol.* 2017, **7**, 51-55.
[4]   U.I. Kramm, I. Herrmann-Geppert, P. Bogdanoff, S. Fiechter, J.Phys.Chem.C 2011, 115, 23417-23427.
[5]   I. Herrmann, U.I. Kramm, J. Radnik, P. Bogdanoff, S. Fiechter, J. Electrochem. Soc. 2009, 156, B1283-1292.
[6]   U.I. Kramm, I. Herrmann-Geppert, S. Fiechter, G. Zehl, I. Zizak, I. Dorbandt, D. Schmeißer, P. Bogdanoff, J. Mater. Chem. A 2014, 2, 2663-2670.
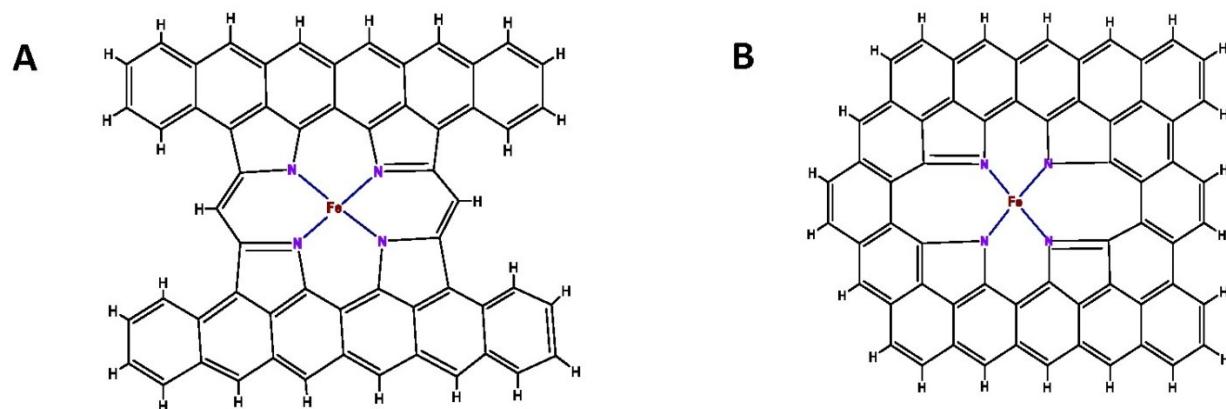
Figure S23: FeN$_4$/C: modeled as a porphyrin-like Fe^{II}N$_4$C$_{12}$,s either hosted in a micropore bridging the « zig-zag » sides of two graphene layers (A) or integrated into a graphene layer (B). Reference [81] in the main text.
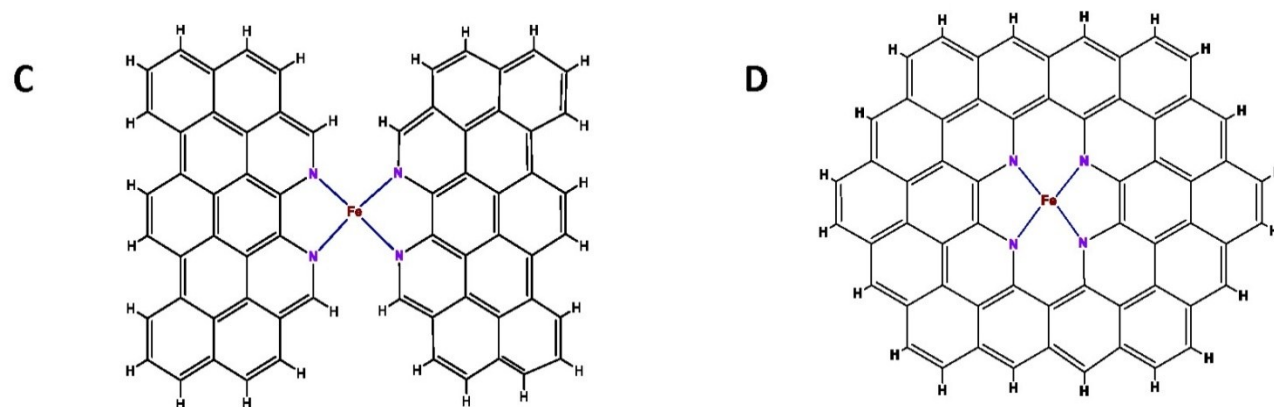

Figure S23: FeN$_{2+2}$/C: modeled as [Fe^{II}(N$_2$R)$_2$]$^{2+}$,s either hosted in a micropore bridging the « armchair » side of two graphene layers (C) or integrated into a graphene layer (D). Reference [81] in the main text.